

REPORT DOCUMENTATION PAGE			Form Approved OMB No. 0704-0188		
Public reporting burden for this collection of information is estimated to average 1 hour per response, including the time for reviewing instructions, searching existing data sources, gathering and maintaining the data needed, and completing and reviewing this collection of information. Send comments regarding this burden estimate or any other aspect of this collection of information, including suggestions for reducing this burden to Department of Defense, Washington Headquarters Services, Directorate for Information Operations and Reports (0704-0188), 1215 Jefferson Davis Highway, Suite 1204, Arlington, VA 22202-4302. Respondents should be aware that notwithstanding any other provision of law, no person shall be subject to any penalty for failing to comply with a collection of information if it does not display a currently valid OMB control number. PLEASE DO NOT RETURN YOUR FORM TO THE ABOVE ADDRESS.					
1. REPORT DATE (DD-MM-YYYY) 09-09-2010		2. REPORT TYPE Journal Article		3. DATES COVERED (From - To)	
4. TITLE AND SUBTITLE Ionizing Shocks in Argon. Part 1: Collisional-Radiative Model and Steady-State Structure (Preprint)				5a. CONTRACT NUMBER	
				5b. GRANT NUMBER	
				5c. PROGRAM ELEMENT NUMBER	
6. AUTHOR(S) J.-L. Cambier (AFRL/RZSS); M.G. Kapper (von Karman Institute)				5d. PROJECT NUMBER	
				5f. WORK UNIT NUMBER 23040256	
7. PERFORMING ORGANIZATION NAME(S) AND ADDRESS(ES) Air Force Research Laboratory (AFMC) AFRL/RZSS 1 Ara Road Edwards AFB CA 93524-7013				8. PERFORMING ORGANIZATION REPORT NUMBER AFRL-RZ-ED-JA-2010-382	
9. SPONSORING / MONITORING AGENCY NAME(S) AND ADDRESS(ES) Air Force Research Laboratory (AFMC) AFRL/RZS 5 Pollux Drive Edwards AFB CA 93524-7048				10. SPONSOR/MONITOR'S ACRONYM(S)	
				11. SPONSOR/MONITOR'S NUMBER(S) AFRL-RZ-ED-JA-2010-382	
12. DISTRIBUTION / AVAILABILITY STATEMENT Approved for public release; distribution unlimited (PA #10442).					
13. SUPPLEMENTARY NOTES For publication in the Journal of Applied Physics.					
14. ABSTRACT A detailed collisional-radiative model is developed and coupled with a single-fluid, two-temperature convection model for the transport of shock-heated argon. The model is used in a systematic approach to examine the effects of the collision cross sections on the shock structure, including the relaxation layer and subsequent radiative-cooling regime. We present a comparison with previous experimental results obtained at the University of Toronto and the Australian National University, which serve as benchmarks to the model. It is shown that ionization proceeds via the ladder-climbing mechanism and is dominant from the upper levels as compared to the metastable states. Taking this into account, the present model is able to accurately reproduce the metastable populations in the relaxation zone measured in previous experiments, which is not possible with a two-step model. Numerical results of the radiative-cooling region are in close agreement with experiments and have been obtained without having to consider radiative transport. In particular, spontaneous free-bound emission to the upper levels together with Bremsstrahlung emission account for nearly all radiative losses; all other significant radiative processes, resulting in a transition into the ground-state, are mostly self-absorbed and have a lesser impact.					
15. SUBJECT TERMS					
16. SECURITY CLASSIFICATION OF:			17. LIMITATION OF ABSTRACT	18. NUMBER OF PAGES	19a. NAME OF RESPONSIBLE PERSON
a. REPORT	b. ABSTRACT	c. THIS PAGE			19b. TELEPHONE NUMBER (include area code)
Unclassified	Unclassified	Unclassified	SAR	16	N/A

Ionizing Shocks in Argon. Part 1: Collisional-Radiative Model and Steady-State Structure (Preprint)

J.-L. Cambier^{1, a)} and M. G. Kapper^{1, 2}

¹⁾ *Air Force Research Laboratory*

10 E. Saturn Blvd.

Edwards AFB, CA 93524, USA

²⁾ *von Karman Institute, Brussels, Belgium.*

(Dated: 9 September 2010)

A detailed collisional-radiative model is developed and coupled with a single-fluid, two-temperature convection model for the transport of shock-heated argon. The model is used in a systematic approach to examine the effects of the collision cross sections on the shock structure, including the relaxation layer and subsequent radiative-cooling regime. We present a comparison with previous experimental results obtained at the University of Toronto and the Australian National University, which serve as benchmarks to the model. It is shown that ionization proceeds via the ladder-climbing mechanism and is dominant from the upper levels as compared to the metastable states. Taking this into account, the present model is able to accurately reproduce the metastable populations in the relaxation zone measured in previous experiments, which is not possible with a two-step model. Numerical results of the radiative-cooling region are in close agreement with experiments and have been obtained without having to consider radiative transport. In particular, spontaneous free-bound emission to the upper levels together with Bremsstrahlung emission account for nearly all radiative losses; all other significant radiative processes, resulting in transitions into the ground-state, are mostly self-absorbed and have a lesser impact. The effects of electron heat conduction are also considered and shown to have a large impact on the electron-priming region immediately behind the shock front; however, the overall effect on induction length is small.

Keywords: Non-Equilibrium Collisional-Radiative Plasma Shocks

I. INTRODUCTION

Non-equilibrium effects in shock-heated plasma provide valuable information such as radiative heat fluxes and associated spectra and are consequently of great interest in research areas such as hypersonic aerodynamics and re-entry flows, as well as other high-enthalpy plasma dynamic applications. Without an energy sink for rotational or vibrational modes or dissociative processes, high shock speeds and temperature jumps are easily obtained with noble gases, making it ideal to study electronic excitation and ionization kinetics towards the validation of collisional-radiative (CR) models. The study of multi-dimensional ionizing shock structures is a first step towards our ultimate objective of a fully-coupled, multi-dimensional flow code for the analysis of complex non-equilibrium plasma, which allows us to test high-order transport solvers to resolve the dynamical nature of the shock structure as well as the detailed kinetics required to solve the non-equilibrium processes in the relaxation region. While the relaxation of shock-heated Argon has been the focus of many numerical investigations, the CR kinetics employed have been modest at best. The first experiments on ionization relaxation in argon were carried out by Petschek and Byron¹, the results of which were used to benchmark theoretical models in subsequent work, while the structure of an ionizing shock wave in

argon was first calculated by Biberman and Yakubov². The majority of computations have been based on the two-step reaction mechanism proposed by Weymann³ in which Argon atoms are initially excited to the lowest excited levels by atom impact from which the valence electron is ejected by further impact, while Wojciechowski and Weymann⁴ showed that the “ladder-climbing” ionization proposed by de Boer and Grimwood⁵ becomes increasingly important as gas temperatures and pressures increase. Coupling of the excitation and ionization kinetics with the fluid dynamics is critical to an accurate analysis of the plasma, and yields further complexity to the problem. For example, McLaren and Hobson⁶ took into account the effect of the boundary layer on the overall relaxation length according to Mirel’s theory^{7,8}. If the boundary layer is small relative to the cross section of the shock tube, it is usually argued that the shock structure can be well approximated as a one-dimensional structure. Nevertheless, we will show in a companion paper that multi-dimensional effects can be important. Similarly, unsteady dynamical effects can result from kinetics and fluid coupling: shock instabilities in argon were noted as far back as Shreffler & Christian⁹, and a previous numerical study¹⁰ demonstrated the effect of an unsteady wave action within the induction zone, and suggested a relevance to the experimental observations of Glass & Liu¹¹. The current work expands on that study by using a more accurate and detailed kinetics model, and demonstrating multi-dimensional and unsteady effects in a companion article.

Below, the focus is placed on the collisional-radiative

^{a)} Electronic mail: jean-luc.cambier@edwards.af.mil

Authors	β^a [m^2/eV]
Harwell and Jahn ¹²	7.1×10^{-23}
Morgan and Morrison ¹³	7.1×10^{-24}
Kelly ¹⁴	1.2×10^{-23}
Wong and Bershader ¹⁵	2.8×10^{-23}
McLaren and Hobson ⁶	2.5×10^{-24}
Merilo and Morgan ¹⁶	1.2×10^{-23}
Wojciechowski and Weymann ⁴	2.1×10^{-23}
Glass and Liu ¹¹	1.0×10^{-23}
Current work	1.0×10^{-24}

TABLE I. Atom-atom cross section parameters for excitation from ground state used in various attempts to reproduce the shock structure in argon.

model itself and the tuning (calibration) of some of the rates and cross-sections, using features of the experimental data from ionizing shocks such as the relaxation length and ionization fraction. In particular, it has been found that atom-atom cross sections for excitation from ground state have the greatest influence on the shock structure and the relaxation length. Since the gas immediately downstream of the shock is not yet ionized, atom-atom collisions behind the shock discontinuity generate the initial priming electrons, which in turn become the dominant ionizing species once sufficient number densities have been obtained. Some values of the atom-atom cross sections used in previous studies, listed in Table I, show that the range of values exceeds an order of magnitude and indicates the relative uncertainty in this particular cross section.

We point out that with the exception of the UTIAS experiments, the shock-tubes were relatively small, the largest having an inner diameter of 5cm. In such shock tubes, the viscous boundary layer becomes a significant portion of the flow, consequently reducing the overall relaxation length. McLaren and Hobson⁶ took this into account using Mirel's transformation and found significant reduction in the atom-impact excitation cross sections in comparison with previous work. Based on the UTIAS data, Kaniel¹⁷ showed that the slope of the electron avalanche was better reproduced by increasing the electron-impact cross sections. This increase in electron-impact excitation cross sections should be accompanied by a decrease in the atom-impact cross sections. In this first article we compute steady-state shock structures and comparison with experiments shows some evidence that the ionizing shock structure can be used to place bounds on the atom-impact cross-sections, while further constraints can be obtained using unsteady effects (discussed in companion article).

II. GOVERNING EQUATIONS

For the conditions of interest, the plasma is sufficiently collisional that a single-fluid continuum model can be as-

sumed. Thermal non-equilibrium effects are accounted for by a multi-temperature (2T) formulation, while the electronic states are transported as individual species, allowing a non-Boltzmann description of the Atomic State Distribution Function (ASDF). The convective transport terms form a hyperbolic system of equations which are written in conservative form and solved with a 3rd-order finite-volume, monotonic numerical scheme. In this article, only steady-state solutions are presented, but the same multi-fluid equations apply to the multi-dimensional and unsteady calculations presented in a second article. The differential form of the governing equations is, in the absence of applied fields (here in 1D):

$$\frac{\partial Q}{\partial t} + \frac{\partial F}{\partial x} = \dot{\Omega} \quad (1)$$

where $\dot{\Omega}$ describes all the collisional-radiative kinetics (as well as energy exchange from elastic collisions) while Q and F are the vectors of conserved variables and fluxes, respectively.

$$Q = \begin{pmatrix} \rho_1 \\ \vdots \\ \rho_n \\ \rho u \\ \rho v \\ \rho w \\ E \\ \rho \hat{s}_e \end{pmatrix}, \quad F = \begin{pmatrix} \rho_1 u \\ \vdots \\ \rho_n u \\ \rho u^2 + p \\ \rho v u \\ \rho w u \\ u H \\ \rho \hat{s}_e u \end{pmatrix}, \quad (2)$$

with,

$$E = \rho \varepsilon_h + \rho \varepsilon_e + \frac{1}{2} \rho \vec{u} \cdot \vec{u} \quad (3)$$

being the total energy density of the plasma and $H = E + p$ the total enthalpy density. In Eq. 3, $\varepsilon_h = \Sigma_{s \neq e} \rho_s \varepsilon_s / \rho$ is the total, specific internal energy density of the heavy fluid. Note also that Eq. 2 contains all 3 components of the velocity (u, v, w) although only one component is non-zero in the 1D geometry studied here. The electron energy equation has been expressed in terms of the entropy function $\hat{s}_e = p_e / \rho^{\gamma_e}$ (cf.¹⁸) in order to maintain a strict divergence form for the convected quantities. Introducing the flux Jacobian $A = \partial F / \partial Q$, Eq. 1 can be written in quasilinear form:

$$\frac{\partial Q}{\partial t} + A \frac{\partial Q}{\partial x} = \dot{\Omega} \quad (4)$$

In the absence of discontinuities (i.e. behind the shock), this form will be used for steady-state solutions, as described below. Closure of the system is obtained with an equation of state (EOS): the plasma is assumed here to be ideal and thermally perfect, together with Dalton's law of partial pressures, i.e. $p = n k_B T$ and $\varepsilon_s = f(T)$, such that $d\varepsilon_s = C_{v,s}(T) dT$ and $C_{v,s}$ is the specific heat

for species s . The total differentials are evaluated as function of the conserved variables Q_k , thus yielding:

$$dp = (\gamma_h - 1) \left[dE + \frac{u^2}{2} d\rho - \vec{u} \cdot d\vec{m} - \sum_{s \neq e} \varepsilon_s d\rho_s - \frac{\rho^{\gamma_e - 1}}{\gamma_e - 1} dS_e \right] + T_h \sum_{s \neq e} R_s d\rho_s + \rho^{\gamma_e - 1} dS_e + (\gamma_e - \gamma_h) \frac{p_e}{\rho} d\rho \quad (5)$$

where we have defined $R_s = k_B/m_s$ and

$$\gamma_h - 1 \equiv \frac{\sum_{s \neq e} \rho_s R_s}{\sum_{s \neq e} \rho_s c_{v,s}} \quad (6)$$

We can also extract the frozen speed of sound,

$$a^2 = \sum \frac{\rho_s}{\rho} \frac{\partial p}{\partial \rho_s} + \left(\varepsilon_h + \varepsilon_e + \frac{p}{\rho} - \frac{u^2}{2} \right) \frac{\partial p}{\partial E} + \hat{s}_e \frac{\partial p}{\partial S_e} \quad (7)$$

where $S_e = \rho \hat{s}_e$. Since the excited levels are convected as individual species, there is no electronic contribution to the internal energy, and only the translational degrees of freedom need be convected with the total energy, viz.

$$\varepsilon_h = \frac{3}{2} T_h \sum_{s \neq e} R_s \quad (8)$$

such that $\gamma_h = \gamma_e \equiv 5/3$.

In the current work, transient effects are neglected and Eq. (4) can be simplified to

$$\frac{dQ}{dx} = A^{-1} \dot{\Omega} \quad (9)$$

An implicit discretization can be obtained via a Taylor series expansion in x of the RHS such that

$$\left(I - \Delta x \frac{\partial A^{-1} \dot{\Omega}}{\partial Q} \right) \Delta Q = \Delta x A^{-1} \dot{\Omega} \quad (10)$$

in which the Jacobian is expanded via

$$J = \frac{(\partial A^{-1} \dot{\Omega})}{\partial Q} = A^{-1} \left(\frac{\partial \dot{\Omega}}{\partial Q} - \frac{\partial A}{\partial Q} A^{-1} \dot{\Omega} \right) \quad (11)$$

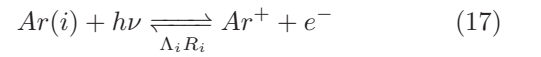
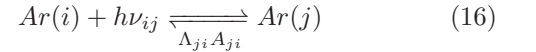
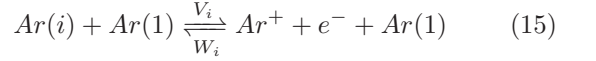
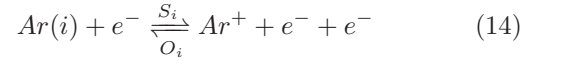
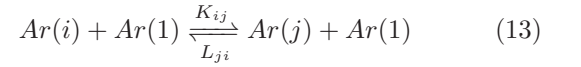
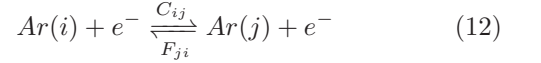
For greater accuracy and stability, the Jacobian has been evaluated analytically. The inverse Jacobian is easily found from its diagonalization $A^{-1} = R\Lambda^{-1}L$, along with $\partial A/\partial Q$.

III. COLLISIONAL-RADIATIVE MODEL

In this section, we describe the collisional-radiative model, for which rates are computed from collision cross sections of the associated processes under the assumption of a Maxwellian electron energy distribution function (EEDF). The CR model used here draws upon the previous work of Vlček¹⁹ and Bultel *et al*²⁰ both of which are specific to argon. The model includes the first 31 excited levels of neutral argon, as well as the ground states of the singly-charged ion. The population numbers of the states beyond those considered here are negligible for the plasma conditions considered, as verified by equilibrium considerations. There is no grouping of levels, as the approach here is to look in detail at the influence of the electronic states, and we presently neglect the influence of molecular Ar_2^+ . As the CR model is being validated on the UTIAS shock tube experiments, any assumptions made herein are based on the plasma conditions of those experiments: this includes number densities up to 10^{24} [m⁻³] and temperatures just above 1 eV.

A. Processes

The processes to be included can be represented by the following equations,



where the rate coefficients are defined by Vlček¹⁹. We adopt the convention $j > i$ such that C_{ij} and K_{ij} represent the rates for excitation from level i to j while F_{ji} , L_{ji} , and Λ_{ji} are the rates for de-excitation from level j to i . The levels considered in the present model include only those up to the $3p^5 3d$ and $3p^5 5s$ manifolds (cf. Table II). This implies that ionization and recombination should proceed from and to only these 31 levels; although levels beyond this manifold are more than 1 eV away from the ionization limit, the combination of small energy gap and large cross-section makes the ionization from these higher levels extremely rapid, certainly occurring with time scales much below the resolution needed in the current research. Thus the 31 lower-lying states considered here contain the bottleneck to the ionization regime and most of the energy into bound states. Note

that neutral argon has two ionization potentials owing to the fact that the levels of argon are split according to two possible configurations for the core angular momentum j_c . As ionization and recombination can proceed only between levels having the same value of j_c , the two lowest lying levels of Ar^+ must be accounted for individually. Thus in the current model, these two levels are treated as separate species and convected as such. Transitions between states with different j_c are considered as well, despite being suppressed relative to identical core transitions.

The forward rate coefficients are computed assuming a Maxwellian electron energy distribution function (EEDF) according to

$$k = \frac{\bar{v}}{(k_B T)^2} \int_{\varepsilon_0}^{\infty} \sigma(\varepsilon) \varepsilon e^{-\varepsilon/k_B T} d\varepsilon \quad (18)$$

where ε_0 is the threshold energy and \bar{v} is the mean thermal velocity,

$$\bar{v} = \left(\frac{8k_B T}{\pi \mu} \right)^{1/2}, \quad (19)$$

with μ the reduced mass. The backward rates are then computed from the principle of detailed balance. For excitation processes this takes the form

$$k_{ji}^{dex} = k_{ij}^{exc} \frac{g_i}{g_j} e^{\varepsilon_{ij}/k_B T} \quad (20)$$

where $\varepsilon_{ij} = \varepsilon_j - \varepsilon_i$ is the energy difference between the upper and lower levels. The temperature in Eq. (20) is that of the impacting species. For ionization and recombination processes, the reverse rates are also computed via detailed balance, leading to:

$$k_i^{rec} = k_i^{ion} \frac{\mathbb{Z}_i}{\mathbb{Z}_+ + \mathbb{Z}_e} \quad (21)$$

where \mathbb{Z}_e is the electron partition function

$$\mathbb{Z}_e = 2 \left(\frac{2\pi m_e k_B T_e}{h^2} \right)^{3/2} \quad (22)$$

Since the electronic states are considered separately, the ratio of partition functions for Ar and Ar^+ is simply

$$\frac{\mathbb{Z}_i}{\mathbb{Z}_+} \approx \frac{g_i}{g_+} e^{I_i/k_B T} \quad (23)$$

with I_i being the ionization potential of the i^{th} excited state, allowing Eq. (21) to be written as

$$k_i^{rec} = k_i^{ion} \frac{g_i}{g_+} \frac{1}{2} \left(\frac{h^2}{2\pi m_e k_B T_e} \right)^{3/2} e^{I_i/k_B T}. \quad (24)$$

Note that the exponential temperature dependence in Eq. (24) is a function of the third body— T is taken to be either the electron or heavy particle temperature for

cases in which the third body is an electron or atom, respectively. We can also use the Boltzmann equilibrium conditions to define an "excitation" temperature which describes the *actual* ratio of the population densities, i.e.:

$$T_{x,ij} \equiv - \left(\frac{k_B}{\varepsilon_{ij}} \ln \left(\frac{n_j/g_j}{n_i/g_i} \right) \right)^{-1}, \quad (25)$$

When the lower level is the ground state, we can simply denote this as $T_{x,j}$. Similarly, we can define a "Saha temperature" to describe the actual ratio of ionized species versus the neutral population, which involves solving for $T_{S,i}$ the equation:

$$\frac{n_+ n_e}{n_i} \frac{g_i}{g_+} = \left(\frac{2\pi m_e k_B T_{S,i}}{h^2} \right)^{3/2} e^{-I_i/k_B T_{S,i}}. \quad (26)$$

In addition to species production rates, the second moment with respect to energy is also necessary to determine the energy production rate for photorecombination (radiative capture) processes,

$$R' = \frac{\bar{v}}{(k_B T)^2} \int_{\varepsilon_0}^{\infty} \sigma(\varepsilon) \varepsilon^2 e^{-\varepsilon/k_B T} d\varepsilon. \quad (27)$$

In practice, all rate coefficients and their derivatives are computed *a priori* and tabulated as a function of temperature.

B. Atom impact processes

Neglecting precursor photo-ionization, atom-atom collisions are the only means for initial electron production behind the viscous shock and yield the priming electrons that eventually trigger inelastic electron collisions. Excitation from ground state in particular plays a significant role in determining the overall induction length, i.e. the distance between shock-front and electron avalanche. In addition, the excitation rates have a profound influence on the dynamics of the simulation. It will be shown in the second article that pressure waves initiated at the electron avalanche are exacerbated for undervalued cross sections while excessive values can lead to over damping of the system. The sharp sensitivity of the convection-kinetics coupling highlights the need for accurate determination of the heavy particle cross sections. We start with Drawin's formula²¹

$$\sigma_{ij}^a(\varepsilon) = 4\pi a_0^2 \left(\frac{I_H}{\varepsilon_{ij}} \right)^2 \frac{m_{\text{Ar}}}{m_H} \xi^2 f_{ij} \times \frac{2m_e}{m_{\text{Ar}} + m_e} \frac{\varepsilon/I_i - 1}{\left(1 + \frac{2m_e}{m_{\text{Ar}} + m_e} (\varepsilon/I_i - 1) \right)^2} \quad (28)$$

where I_H is the ionization potential of the hydrogen atom and $\xi = 6$ is the number of optical electrons of argon. For

i	$\varepsilon(i)$ [eV]	g_i	j_c	$n\ell[K]_J$	i	$\varepsilon(i)$ [eV]	g_i	j_c	$n\ell[K]_J$
1	0	1	1.5	[Mg]3p ⁶	18	13.903	5	1.5	3d[3/2] ₂
2	11.548	5	1.5	4s[3/2] ₂	19	13.979	9	1.5	3d[7/2] ₄
3	11.624	3	1.5	4s[3/2] ₁	20	14.013	7	1.5	3d[7/2] ₃
4	11.723	1	0.5	4s'[1/2] ₀	21	14.063	5	1.5	3d[5/2] ₂
5	11.828	3	0.5	4s'[1/2] ₁	22	14.068	5	1.5	5s[3/2] ₂
6	12.907	3	1.5	4p[1/2] ₁	23	14.090	3	1.5	5s[3/2] ₁
7	13.076	7	1.5	4p[5/2] ₃	24	14.099	7	1.5	3d[5/2] ₃
8	13.095	5	1.5	4p[5/2] ₂	25	14.153	3	1.5	3d[3/2] ₁
9	13.153	3	1.5	4p[3/2] ₁	26	14.214	5	0.5	3d'[5/2] ₂
10	13.172	5	1.5	4p[3/2] ₂	27	14.234	5	0.5	3d'[3/2] ₂
11	13.273	1	1.5	4p'[1/2] ₀	28	14.236	7	0.5	3d'[5/2] ₃
12	13.283	3	0.5	4p'[3/2] ₁	29	14.241	1	0.5	5s'[1/2] ₀
13	13.302	5	0.5	4p'[3/2] ₂	30	14.255	3	0.5	5s'[1/2] ₁
14	13.328	3	0.5	4p'[1/2] ₁	31	14.304	3	0.5	3d'[3/2] ₁
15	13.480	1	0.5	4p'[1/2] ₀	∞	15.760	4	1.5	[Mg]3p ⁵
16	13.845	1	1.5	3d[1/2] ₀	∞'	15.937	2	0.5	[Mg]3p ⁵
17	13.864	3	1.5	3d[1/2] ₁					

TABLE II. Argon levels considered in current CR model.

i	j	β_{ij}^* [m ² /eV]	f_{ij}
1	3	1.10×10^{-23}	6.78×10^{-02}
1	5	3.95×10^{-23}	2.56×10^{-01}
1	17	9.58×10^{-26}	1.00×10^{-03}
1	23	3.10×10^{-24}	3.40×10^{-02}
1	25	8.55×10^{-24}	9.51×10^{-02}
1	30	1.59×10^{-24}	1.80×10^{-02}
1	31	6.92×10^{-24}	7.94×10^{-02}

TABLE III. Atom impact excitation parameters for allowed transitions from ground state Ar.

i	j	β_{ij}^* [m ² /eV]
2	3	1.79×10^{-24}
2	4	4.80×10^{-26}
2	5	4.80×10^{-26}
3	4	4.80×10^{-26}
3	5	4.80×10^{-26}
4	5	1.79×10^{-24}

TABLE IV. Atom impact excitation parameters for intra-4s transitions.

the energy ranges under consideration, Eq. (28) is well-approximated by a linear function,

$$\sigma_{1j}^a(\varepsilon) = \beta_{1j}^*(\varepsilon - \varepsilon_{1j}), \quad (29)$$

where

$$\beta_{1j}^* = 4\pi a_0^2 \frac{(I_H)^2}{\varepsilon_{1j}^3} \xi^2 f_{1j} \frac{2m_e}{m_H} \quad (30)$$

The inner 3p⁵4s manifold transitions, however, take the form²⁰

$$\sigma_{ij}^a(\varepsilon) = \beta_{ij}^* \frac{\varepsilon - \varepsilon_{ij}}{\varepsilon_{ij}^{2.26}} \quad (31)$$

The linear β -parameters are provided in Tables III and IV. Note the relative strength of $\Delta j_c \equiv 0$ transitions compared to the $4s - 4s'$ ($\Delta j_c \neq 0$) transition.

Less sensitive are the ionization cross sections—we remark here that decreasing these values by an order of magnitude did not have any significant effect on the induction length or flow dynamics. The cross section for ionization from ground state argon is taken from²²,

$$\sigma_1^a(\varepsilon) = 1.8 \times 10^{-25} (\varepsilon - 15.760)^{1.3} \text{ [m}^2\text{]}, \quad (32)$$

while the formula of Drawin has been applied for all other levels (for further details, the reader is directed to²⁰ and¹⁹ and the references therein).

$$\sigma_i^a(\varepsilon) = 4\pi a_0^2 \left(\frac{I_H}{I_i} \right)^2 \frac{m_{Ar}}{m_H} \xi^2 \times \frac{2m_e}{m_{Ar} + m_e} \frac{\varepsilon/I_i - 1}{\left(1 + \frac{2m_e}{m_{Ar} + m_e} (\varepsilon/I_i - 1) \right)^2}. \quad (33)$$

C. Electron impact processes

Once a sufficient number of priming electrons have been generated by heavy particle impact and their temperature increased by thermalization, electron impact processes begin to become important and eventually dominate the kinetics. The cross sections for electron-impact excitation are due to Zatsarinny and Bartschat^{23,24}. These include excitation from the ground and 4s levels to all levels below the 5p manifold. For all

parameter for Eq. (36)	Valence electron shell			
	s	p	d	f
a	1.06	2	3/2	3/2
b	0.23	1	3	1
c	1	1	2/3	2/3
d	1	1	1	1

TABLE V. Electron-impact ionization parameters as taken from²⁶.

Valence electron		
shell, $n\ell$	$r_{n\ell}$ [Å]	$g_{n\ell} \times I_{n\ell}$ [eV]
4s	2.49	7.40
5s	6.35	6.35
4p	3.40	31.00
3d	4.36	13.60

TABLE VI. Radii of Ar valence electron and reduced weighting factors for $\xi = 1$ as taken from²⁶ and²⁵.

other transitions, Drawin's formulas

$$\sigma_{ij}^e(\varepsilon) = 4\pi a_0^2 \frac{(u_{ij} - 1)}{u_{ij}^2} \begin{cases} \alpha_{ij}^A f_{ij} \left(\frac{I_H}{\varepsilon_{ij}} \right)^2 \ln(1.25\beta_{ij} u_{ij}) \\ \alpha_{ij}^P \\ \alpha_{ij}^S \left(\frac{u_{ij}+1}{u_{ij}^3} \right) \end{cases} \quad (34)$$

have been used systematically with $\alpha_{ij}^A f_{ij} = 1$, $\alpha_{ij}^P = 1$, and $\alpha_{ij}^S = 1$.

Cross sections for electron-impact ionization from the excited levels have been determined based on the work of Deutsch *et al.*²⁵:

$$\sigma_i(\varepsilon) = g_{n\ell} \pi r_{n\ell}^2 \xi_{n\ell} f(\varepsilon) \quad (35)$$

where $g_{n\ell}$ are the reduced weighting factors, $r_{n\ell}$ are the radii of the valence electron, and

$$f_i(\varepsilon) = d \frac{I_i}{\varepsilon} \left(\frac{\varepsilon/I_i - 1}{\varepsilon/I_i + 1} \right)^a \times \left[b + c \left(1 - \frac{I_i}{2\varepsilon} \right) \ln(2.7 + (\varepsilon/I_i - 1)^{1/2}) \right] \quad (36)$$

The necessary parameters for Eqs. (35) and (36) are given in Tables V and VI.

Particular attention should be paid when considering ionization and recombination in plasmas defined by relatively high densities, as non-ideal effects for which interactions between particles can lead to an effective lowering of the ionization potential. As a consequence, the rates must be considered as functions of pressure as well. Griem²⁷ used Debye theory to predict a decrease in the ionization potential that is inversely proportional to the Debye length,

$$\Delta\varepsilon_{\infty,m} = \frac{(m+1)e^2}{4\pi\epsilon_0\lambda_D}, \quad (37)$$

with the Debye length (neglecting the effect of ions),

$$\lambda_D = \left(\frac{\epsilon_0 k_B T_e}{N_e e^2} \right)^{1/2}. \quad (38)$$

For the shock tube conditions under consideration, the lowering of the ionization potential was found to be relatively small (0.08), yielding a drop of 0.08 eV for an electron temperature of 1 eV and number density of 10^{23} m^{-3} . As a result, the effects of pressure ionization were neglected.

D. Photorecombination

In the absence of a third body, the energy released in recombination is liberated as radiation. Photorecombination is a significant loss mechanism and plays an important role in radiative cooling. The cross section for photorecombination can be found from the cross section for photoionization under equilibrium conditions²⁸,

$$\sigma_{c,i}(\nu) = \frac{g_n}{g_+} \frac{h^2 \nu^2}{m_e^2 v_e^2 c^2} \sigma_{\nu,i}(\nu). \quad (39)$$

Utilizing the relation $h\nu = m_e v^2/2 + \varepsilon_i = \varepsilon + \varepsilon_i$, the cross section associated with the ground state is given by

$$\sigma_1(\varepsilon) = \frac{g_1}{g_+} \frac{(\varepsilon + \varepsilon_1)^2}{2\varepsilon m_e c^2} \times \begin{cases} 3.5 \times 10^{-21} & 0 \leq \varepsilon \leq 2I_H - \varepsilon_1 \\ 2.8 \times 10^{-20} \left(\frac{I_H}{\varepsilon + \varepsilon_1} \right)^3 & \varepsilon > 2I_H - \varepsilon_1 \end{cases} \quad (40)$$

while all others are computed using

$$\sigma_i(\varepsilon) = \gamma_i(n_{pqn,\ell}) \frac{g_i}{g_+} \frac{(\varepsilon + \varepsilon_i)^2}{2\varepsilon m_e c^2} 10^{-22} \times \begin{cases} 2 & 0 \leq \varepsilon \leq 0.59I_H - \varepsilon_1 \\ 7.91 \left(\frac{\varepsilon_i}{I_H} \right)^{5/2} \left(\frac{I_H}{\varepsilon + \varepsilon_i} \right)^3 & \varepsilon > 0.59I_H - \varepsilon_i \end{cases} \quad (41)$$

The parameter $\gamma_i(n_{pqn,\ell})$ takes the values 0.0763, 0.0458, 0.0305, and 0.0915 for $i = 2, 3, 4$, and 5, respectively¹⁹.

Based on nominal shock tube plasma conditions, an estimation of the mean-free path for photoionization from the ground state is on the order of 100 μm . In the case of the 4s levels, their lower populations combined with reduced cross sections result in mean-free paths on the order of 1 m . Consequently, free-bound radiation into the ground state is assumed to be locally absorbed, while the plasma is assumed to be optically thin to transitions from the excited levels.

lower level	upper level	mean-free path [m]
$3p^6$	$4s[3/2]_1$	3.59×10^{-2}
$3p^6$	$4s'[1/2]_1$	9.47×10^{-3}
$3p^6$	$3d[1/2]_1$	2.41
$3p^6$	$5s[3/2]_1$	7.11×10^{-2}
$3p^6$	$3d[3/2]_1$	2.54×10^{-2}
$3p^6$	$5s'[1/2]_1$	1.34×10^{-1}
$3p^6$	$3d'[3/2]_1$	3.05×10^{-2}

TABLE VII. Estimated mean-free paths for bound-bound transitions to ground state for $T = 1$ eV and $n_{3p^6} = 10^{24} \text{ m}^{-3}$.

E. Bound-bound transitions

Bound-bound transitions are another significant source of radiative cooling of the plasma. The photo-absorption cross section for a given bound-bound transition may be estimated by²⁸,

$$\sigma_{ij} = \frac{1}{\nu_{ij}} \int \sigma_{\nu,ij} d\nu = 2.65 \times 10^{-6} \frac{f_{ij}}{\nu_{ij}} [\text{m}^2] \quad (42)$$

where the absorption oscillator strength is given by

$$f_{ij}^{\text{abs}} = \frac{g_j}{g_i} \frac{A_{ji}}{3\gamma}. \quad (43)$$

Contributions to the parameter γ have been assumed to result from a combination of natural and pressure line broadening,

$$\gamma = \gamma_{\text{nat}} + \gamma_{\text{col}} \quad (44)$$

given by

$$\gamma_{\text{nat}} = \frac{8\pi^2 e^2 \nu^2}{3mc^3} = 2.47 \times 10^{-22} \nu^2 [\text{s}^{-1}] \quad (45)$$

and

$$\gamma_{\text{col}} = \frac{2}{\tau_{\text{col}}} = 2\sigma\bar{\nu}n \quad (46)$$

respectively. The collision time τ_{col} and the collision cross section σ have been tallied for all argon-argon collisions. The radiation cross sections Eq. (42) have been estimated using the oscillator strengths and transition probabilities from²⁹ along with representative plasma conditions of the shock tube experiments. The resulting mean-free paths for bound-bound transitions to ground state given in Table VII are below the length scales of the shock tube dimensions and induction length for most of the levels. It has therefore been assumed that all bound-bound radiation to the ground level from the excited states is absorbed. For all other transitions, the mean-free path is several orders of magnitude greater than the dimensions of the shock tube and the associated radiation is assumed to escape. This simplified treatment of the radiation will be re-examined in a future study and compared with a radiation transport model.

F. Bremsstrahlung emission

Free-free transitions have been incorporated in the model via Kramer's formula²⁸ for *Bremsstrahlung* emission. Thus the corresponding term in the vector $\dot{\Omega}$ of Eq. 1 is:

$$\begin{aligned} \left[\frac{dE_e}{dt} \right]_{\text{CR}} &= -\frac{16\pi^2}{3\sqrt{3}} \frac{\bar{\nu}_e Z_{\text{eff}}^2 e^6 \bar{g}}{m_e h (4\pi\epsilon_0 c)^3} n_+ n_e \\ &= -1.42 \times 10^{-40} Z_{\text{eff}}^2 T_e^{1/2} n_+ n_e \quad [\text{J/m}^3 \cdot \text{s}] \end{aligned} \quad (47)$$

where \bar{g} is the gaunt factor (here taken to be unity) and the effective charge Z_{eff}^2 is taken to be 1.67¹¹. Bremsstrahlung emission resulting from neutral atoms is 1–2 orders of magnitude less than for ions and has therefore been neglected²⁸. The plasma is assumed to be optically thin to all Bremsstrahlung emission.

G. Elastic collisions

Elastic collisions are incorporated into the CR implicit solver as well. This strong coupling permits more accurate and stable calculations. The energy transfer between electrons and heavy particles is computed from

$$\left[\frac{dE_e}{dt} \right]_{\text{CR}} = - \left[\frac{dE_h}{dt} \right]_{\text{CR}} = n_e n_n \frac{3}{2} k_B (T_h - T_e) \delta k_{eh} \quad (48)$$

where $\delta = 2m_e/m_{Ar}$ and $k_{eh} = k_{ei}, k_{en}$ for Coulomb and elastic collisions with neutral argon respectively. For the latter, the theoretical cross section of McEachran and Stauffer³⁰ have been utilized which are reproduced in Table VIII. The Coulomb collision rates, \bar{k}_{ei} , have been computed using the energy-averaged properties³¹,

$$\bar{k}_{ei} = \bar{\nu}_e \bar{\sigma}_{ei} \quad (49)$$

$$\bar{\sigma}_{ei} = 5.85 \times 10^{-10} \frac{\ln \Lambda}{T_e^2} [\text{m}^2] \quad (50)$$

where $\bar{\sigma}_{ei}$ is the momentum-averaged cross section, and

$$\Lambda = 1.24 \times 10^7 \left(\frac{T_e^3}{n_e} \right)^{1/2} \quad (51)$$

is the Coulomb logarithm.

ε [eV]	σ_{en} [10^{20} m ²]	ε [eV]	σ_{en} [10^{20} m ²]
0.01	4.0231	0.41	0.3396
0.03	2.3425	0.51	0.5349
0.05	1.5247	0.61	0.7381
0.07	1.0261	0.71	0.9318
0.09	0.6998	0.81	1.1139
0.13	0.3291	0.91	1.2835
0.17	0.1599	1.00	1.4280
0.19	0.1198	1.50	2.1438
0.21	0.0983	2.00	2.8318
0.23	0.0917	3.00	4.4046
0.25	0.0969	4.00	6.3502
0.29	0.1316	5.00	8.6317
0.31	0.1573	7.50	14.6559
0.32	0.1724	10.00	17.8325

TABLE VIII. Momentum transfer cross sections for electron-neutral collisions³⁰.

H. Rate equations

The rate equations for the ground and excited states of neutral argon are given by

$$\begin{aligned}
\frac{\partial n_k}{\partial t} = & \sum_{i < k} n_i (n_e C_{ik} + n_1 K_{ik}) \\
& - \sum_{j < k} n_k (n_e F_{kj} + n_1 L_{kj} + \Lambda_{kj} A_{kj}) \\
& - \sum_{j > k} n_k (n_e C_{kj} + n_1 K_{kj}) \\
& + \sum_{i > k} n_i (n_e F_{ik} + n_1 L_{ik} + \Lambda_{ik} A_{ik}) \\
& + n_+ n_e (n_1 W_k + n_e O_k + \Lambda_k R_k) \\
& - n_k (n_e S_k + n_1 V_k)
\end{aligned} \tag{52}$$

while those for the two ground states of singly-ionized argon take the form

$$\begin{aligned}
\frac{\partial n_+}{\partial t} = & \sum_i n_i (n_e S_i + n_1 V_i) \\
& - n_+ n_e \sum_i (n_1 W_i + n_e O_i + \Lambda_i R_i)
\end{aligned} \tag{53}$$

The energy rate equations are most easily split into one for the heavy-particle energy,

$$\frac{\partial E_h}{\partial t} = n_1 \sum_i \sum_{j > i} \varepsilon_{ij} (n_j L_{ji} - n_i K_{ij}) \tag{54}$$

$$+ n_1 \sum_i I_i (n_e n_+ W_i - n_i V_i) \tag{55}$$

$$- 3\rho_e n_n k_B (T_h - T_e) \frac{k_{en}}{m_{Ar}} \tag{56}$$

$$- 3\rho_e n_+ k_B (T_h - T_e) \frac{\bar{k}_{ei}}{m_{Ar+}} \tag{57}$$

as well as that for the electron energy,

$$\frac{\partial E_e}{\partial t} = n_e \sum_i \sum_{j > i} \varepsilon_{ij} (n_j F_{ji} - n_i C_{ij}) \tag{58}$$

$$+ n_e \sum_i I_i (n_e n_+ O_i - n_i S_i) \tag{59}$$

$$- n_e n_+ \sum_i \Lambda_i R'_i \tag{60}$$

$$- n_+ n_e \frac{16\pi^2}{3\sqrt{3}} \frac{\bar{v}_e Z_{\text{eff}}^2 e^6 \bar{g}}{m_e h (4\pi\epsilon_0 c)^3} \tag{61}$$

$$+ 3\rho_e n_n k_B (T_h - T_e) \frac{k_{en}}{m_{Ar}} \tag{62}$$

$$+ 3\rho_e n_+ k_B (T_h - T_e) \frac{\bar{k}_{ei}}{m_{Ar+}} \tag{63}$$

These equations are solved simultaneously with a backward-Euler method, i.e. are implicit in time.

IV. VALIDATION/CALIBRATION

A. Atom Impact Calibration

Using dual-wavelength interferometry, the UTIAS experiments¹¹ were able to provide detailed insight of the shock structure in terms of the total mass density of the plasma as well as the electron number density. From this it was possible to obtain not only the relaxation length ℓ and the peak ionization fraction α , but also the slopes of the plasma properties in the electron avalanche and in the radiative-cooling region, which could be used to validate the CR model. Experimental conditions for the seven UTIAS cases studied here are provided in Table IX. Digitization of the interferometry snapshots have yielded results of the relaxing shock which are presented in terms of total mass density ρ , electron number density n_e , and ionization fraction α in the provided references. As there exists a fair amount of uncertainty associated with the atom-atom excitation cross sections σ^a , these were varied until an acceptable agreement between the theoretically-predicted and experimentally-observed relaxation lengths was achieved. Exact agreement for all cases could not be achieved with a fixed value for σ^a . However, good agreement was obtained for the intermediate cases, corresponding to Mach numbers 14.7, 15.9, and 16.1, the results of which are summarized in Table X.

As mentioned in Section IIIB, the atom-atom impact excitation cross sections have been approximated as linear functions of energy as based on the model of Drawin. Tuning these cross sections was therefore a matter of modifying the slopes of the parameter β . As a result, the values of β_{1j}^* in Eq. 29 were reduced by a factor of 25, and are summarized in Table XI. In comparison with values previously obtained in the literature (cf. Table I), it is evident that the cross sections used here are at the

Case	Ma _s	p _o [torr]	T _o [K]	Ref.
1	15.9	5.14	293.6	Tang (1977)
2	16.1	5.15	295.9	Tang (1977)
3	16.5	5.12	296.6	Brimelow (1974)
4	13.0	5.01	296.6	Whitten (1977)
5	17.2	2.06	297.8	Bristow (1971)
6	13.6	5.12	297.0	Brimelow (1974)
7	14.7	4.08	297.8	Glass & Liu (1978)

TABLE IX. Shock tube cases studied at UTIAS.

Case	Experiment		Theory	
	ℓ _* [cm]	α _*	ℓ _* [cm]	α _*
1	2.00	0.140	2.00	0.133
2	1.90	0.150	1.80	0.141
3	1.80	0.160	1.53	0.154
4	8.90	0.060	10.9	0.058
5	1.60	0.180	2.31	0.180
6	8.00	0.074	6.96	0.072
7	4.40	0.106	4.35	0.103

TABLE X. Comparison between experimental and steady-state numerical relaxation lengths for ionizing shock in argon.

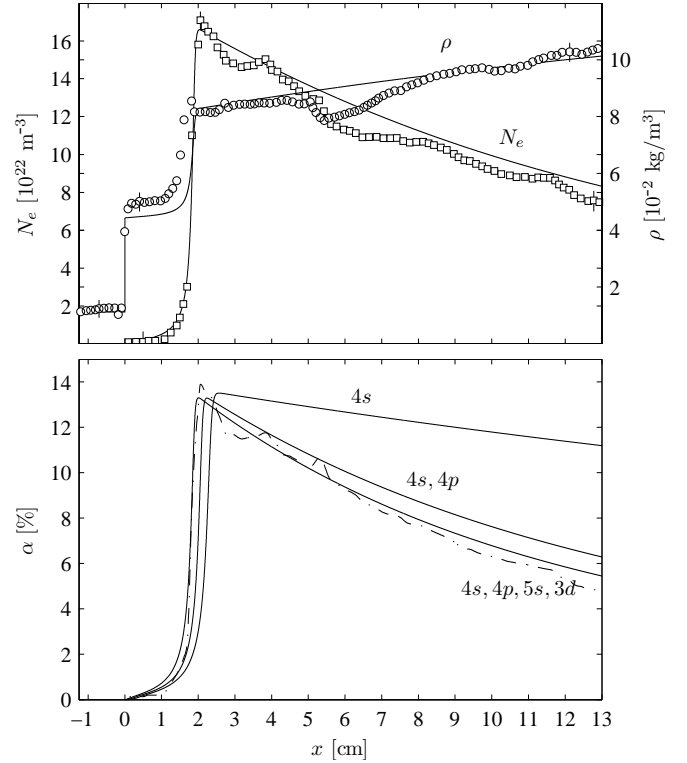
lower end of the spectrum, matching most closely with the values obtained by McLaren and Hobson⁶.

B. Relaxation Region

The results using these cross sections for case 1 given in Fig. 1 show excellent agreement with the experimental results. In an effort to quantify the influence of the upper levels on the overall shock structure, simulations were first performed taking into account the 4s manifold of Ar exclusively, followed by systematic inclusion of higher manifolds, including the 4p, 5s and 3d. Numerical results obtained with levels of only the 4s manifold given in Figure 1 show satisfactory prediction of the induction length, but poor reproduction of the radiative cooling region as indicated by the slow drop-off in electron number density, indicating an under-prediction in radiative losses. This is as expected as the plasma has been as-

i	j	β _{ij} [*] [m ² /eV]
1	3	9.35 × 10 ⁻²⁵
1	5	3.36 × 10 ⁻²⁴
1	17	8.14 × 10 ⁻²⁷
1	23	2.64 × 10 ⁻²⁵
1	25	7.27 × 10 ⁻²⁵
1	30	1.35 × 10 ⁻²⁵
1	31	5.88 × 10 ⁻²⁵

TABLE XI. Tuned atom impact excitation parameters for allowed transitions from ground state Ar.

FIG. 1. Ionizing shock structure as detailed by (a) ρ and n_e , and (b) α for case 1: $p_o = 5.14$ torr, $T_o = 293.6$ K, $Ma = 15.9$.

sumed to be optically-thick for all transitions to ground state Ar (cf. Sections III D, III E), resulting in no radiative losses due to bound-bound transitions since intra-4s transitions are forbidden. As a result, all radiative losses in this case were due to free-free and free-bound transitions only. Also apparent is the effect of the upper levels on the induction length—addition of the upper levels promotes ladder climbing in the induction zone, facilitating ionization and onset of the electron avalanche. It should be noted that the ionization fractions as derived from the experimental data for this particular case, $Ma = 15.9$, as well as for the case of $Ma = 16.1$ in¹¹ do not coincide with the respective total mass and electron number densities provided. As a consequence, the experimental ionization fractions plotted for comparison have been obtained directly from the plasma densities.

Details of the electron and heavy-particle temperature profiles along with the Boltzmann and Saha equivalence temperatures provided in Figure 2 help illustrate the influence of the various CR processes and to separate the shock structure into five distinct regions. The first region, easily identifiable by a sharp spike in electron temperature just behind the compression shock, indicates the initial production of priming electrons. The spike is quickly followed by a dip in electron temperature (region II), signaling a shift from heavy-particle dominated kinetics to electron-impact processes. The excitation temperatures based on a Boltzmann distribution (see Eq. (25)) and

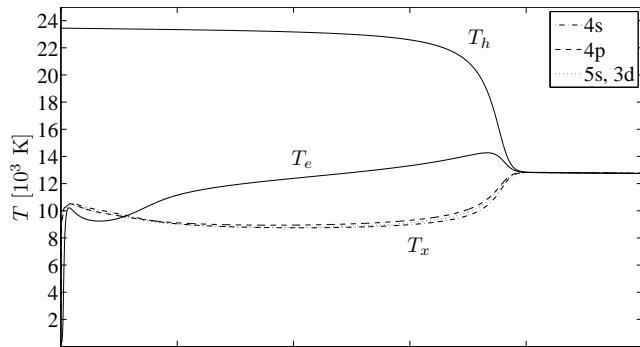


FIG. 2. Plot of heavy-particle and electron temperatures along with excitation temperatures of excited states for Mach 15.9 shock.

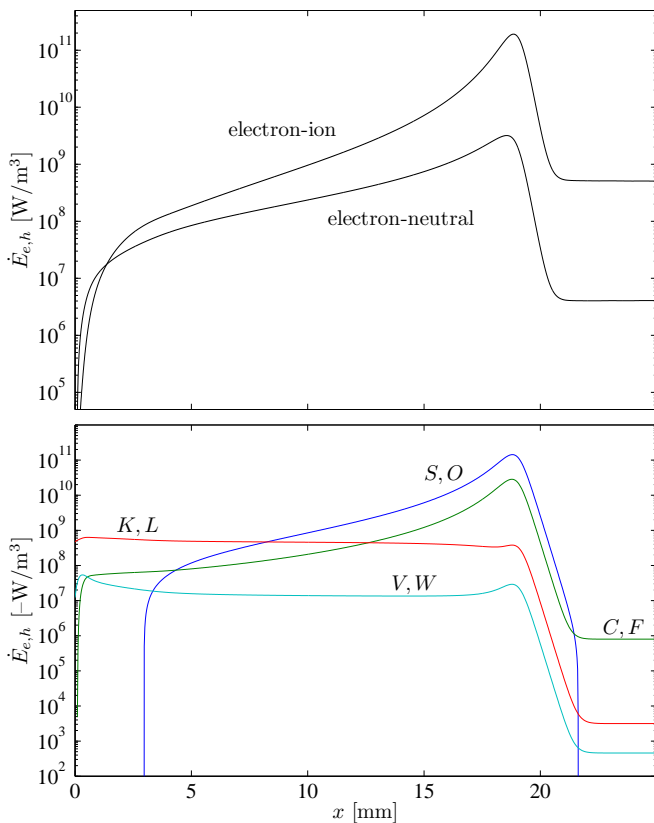


FIG. 3. Net power transfer due to (a) elastic and (b) inelastic collisions.

measured with respect to the ground state, surpass the electron temperature, indicating over-population of the excited states and confirming that the priming electrons are generated via $Ar-Ar$ inelastic collisions. The evolution of T_e presumably results from a competition between elastic exchanges with the hot atoms and energy loss due to excitation and ionization. To confirm this interpretation, we monitored the effective rates of change to the electron energy and density due to both elastic and inelastic processes, shown in Figure 3. It is clear that while elastic collisions gradually increase the electron energy,

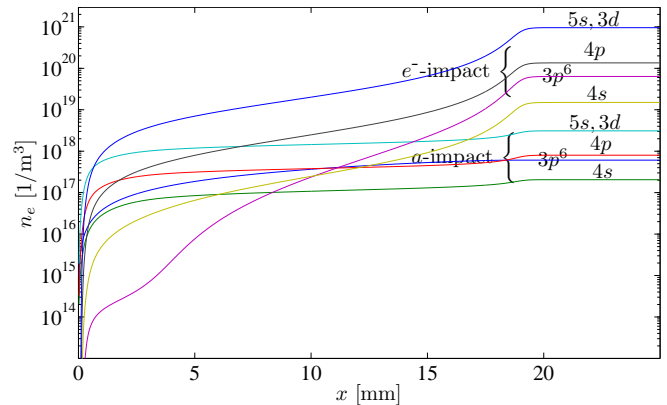


FIG. 4. Accumulated net electron number density production separated by manifold.

inelastic collisions act as a significant energy sink term. The point at which the electron temperature starts to dip (start of region II) corresponds to that for which electron impact ionization from the upper levels starts to dominate over the heavy-particle impact process (compare C,F and V,W curves in Fig. 3). After this small drop, the electron temperature recovers and increases steadily as energy is transferred from the heavy-particles to the free electrons at a slightly higher rate than which the electrons lose energy through inelastic collisions. In this region (III), electron production begins to ramp up exponentially, triggering rapid thermalization with the heavy-particles. Note that the excitation temperature declines as well, and stabilizes significantly below the electron temperature. This can be explained by rapid ionization from the excited levels, causing under-population of the excited levels, and hence the deviation from T_e . It is also worth pointing out that the start of this region approximately coincides with the dominance of electron-impact ionization (compare S,O and V,W curves) and soon after the dominance of electron-ion thermalization. Thus, as more electrons (and ions) are generated by electron impact ionization, the rate of thermalization increases, which further enhances the rate of electron production. This highly non-linear process inevitably results in the electron avalanche (region IV), when sufficient electrons are produced to affect the temperature of the neutral bath itself, which rapidly decays. The avalanche results in complete thermalization between the heavy-particles and electrons (region V), as the energy reserves of the heavy particles becomes exhausted. All levels finally reach Boltzmann and Saha equilibrium and at that point the plasma is well-described by a single temperature.

Note that the spread of excitation temperatures throughout the shock structure is quite small, indicating a Boltzmann equilibrium among the excited levels with respect to the ground state, due to a rapid exchange between the excited levels. Thus, the plasma may be well approximated by a three-temperature model under such conditions¹⁰.

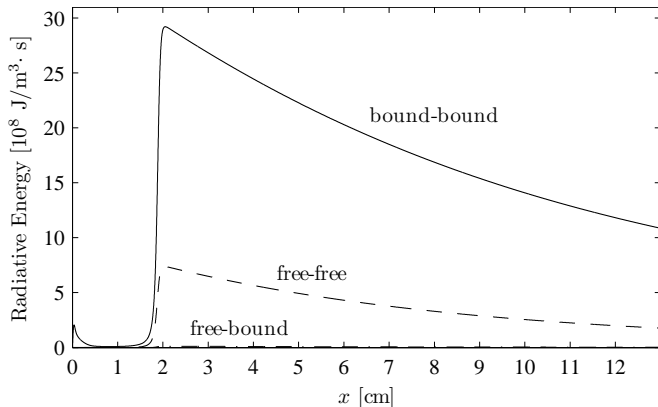
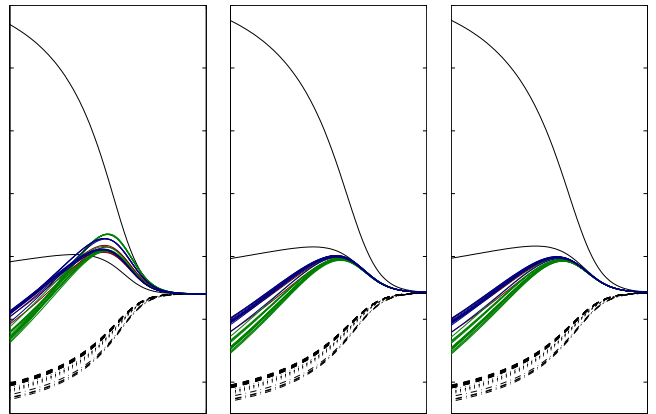


FIG. 5. Individual contributions to radiative losses

Since the evolution of the electron temperature follows from the balance between thermalization and inelastic losses, the elastic collisions can have a significant effect on the overall relaxation length—their inclusion requires reduction of the atom-impact cross sections by one half to obtain lengths comparable to cases when such collisions are not considered—and proper treatment of the Coulomb collisions is required. The electron production rates shown in Fig. 4 corroborate the mechanism of production of priming electrons from atom-impact ionization which is then quickly eclipsed by electron-impact processes. Furthermore we verify that ionization proceeds most prevalently from the upper levels via the ladder-climbing mechanism. Inelastic collisional exchange between the excited levels is very fast, leading to a Boltzmann distribution with a nearly common T_x .

The radiative power density is shown in Fig. 5(a). Comparing with the collisional rates of Fig. 3, it can be seen that the power is much smaller in the induction zone ($< 2\text{cm}$) as expected, since the electron density is low. At and behind the avalanche, the overall radiation is increased by several orders of magnitude, with the line transitions dominating the radiative losses. However, the strongest lines are for transitions to the ground state, which are assumed self-absorbed (escape factor $\Lambda_{ij} = 0$). If we account for the self-absorption of both the bound-bound and free-bound transitions to the ground state, the *net* radiative power would become much smaller.

Figure 6 illustrates the effects on the avalanche region if the collisional time scales are not fully resolved. For a coarse discretization, the Saha temperatures of the higher states (green, red and blue solid curves) overshoot T_e and relaxes with T_h , indicating over-ionization in the avalanche region *w.r.t.* electron-impact collisions. Since the electron-impact cross sections are larger than their atom-impact counterparts, the Saha temperature should instead relax to T_e as in 6(c). This unphysical behavior disappears once the fast-time scales are resolved (which is equivalent to spacing resolution for the steady-state calculation). Because the higher states have a low absolute population and exchange little energy with the contin-

FIG. 6. Effect of discretization on Saha temperature: (a) $\Delta x = 25\mu\text{m}$ (b) $\Delta x = 2.5\mu\text{m}$ (c) $\Delta x = 0.25\mu\text{m}$.

uum (small ionization potential), the solution remains stable and the basic shock structure unchanged even if under-resolved.

C. Electron Heat Conduction

Due to the high thermal velocities of the free electron gas combined with large temperature gradients, the rates of electron heat conduction in the relaxation region can be significant. The change in the conservative variables may be expressed in operator-split form as

$$\left. \frac{\partial E_e}{\partial t} \right|_{\text{cond}} = \frac{\partial}{\partial x} \left(\kappa_e \frac{\partial T_e}{\partial x} \right), \quad (64)$$

with the form of the electron thermal conductivity taken as³²

$$\kappa_e = \left(2 + \frac{1}{\gamma_e - 1} \right) \frac{5n_e k_b^2 T_e}{2m_e \nu_e} \quad (65)$$

where the total electron collision frequency includes all species, $\nu_e = \nu_{ee} + \nu_{ei} + \nu_{en}$. We have used both the energy-averaged electron-electron and electron-ion collision frequencies,

$$\bar{\nu}_{ei} = n_i \frac{4\sqrt{2}\pi}{3} \left(\frac{m_e}{k_B T_e} \right)^{3/2} \left(\frac{e^2}{4\pi\epsilon_0 m_e} \right)^2 \ln \Lambda, \quad (66)$$

and $\nu_{ee} = 2\nu_{ei}$, along with the electron-neutral collision frequency $\bar{\nu}_{en} = n_h k_{en}$,

$$k_{en} = \frac{\bar{\nu}}{(k_B T_e)^2} \int_0^\infty \sigma(\epsilon) \epsilon e^{-\epsilon/k_B T_e} d\epsilon \quad (67)$$

Eq. (64) was solved implicitly in x using operator-splitting, assuming the shock front to be adiabatic. This is consistent with our assumption that there are no precursor electrons. At the opposite end of the domain, where the slope of the radiative-cooling regime dT/dx

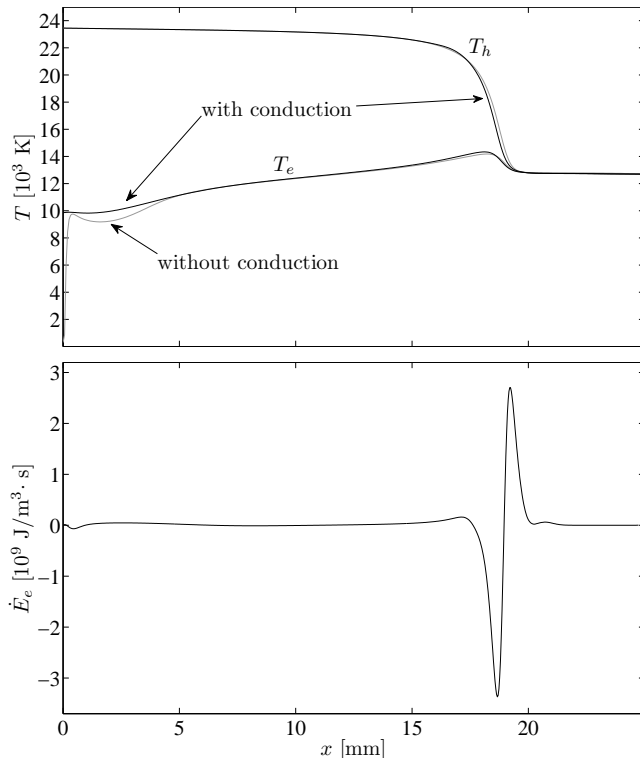


FIG. 7. Effect of electron heat conduction on temperature in the relaxation region.

is dominated by radiative processes, we have fixed the slope of T_e , thereby assuming a constant heat flux. The effect of heat conduction applied to case 1 can be seen in Fig. 7. Most notably, the sharp gradient in T_e just behind the shock has been eliminated followed by a large reduction in the trough created by electron-impact processes following the overshoot. Since the electron density is quite low in this priming region, the amount of energy diffused has a trivial effect on the overall relaxation length and temperature profiles, which remain essentially unchanged. It is clear from comparison of Figures 7(b) and 3(a) that the energy transferred through conduction is roughly two orders of magnitude lower than the energy transferred through Coulomb collisions. Nevertheless, the smoothing of the electron temperature profile in the priming region can be important from a numerical standpoint: because of the highly nonlinear dependence of the kinetics on temperature, the sharp gradient imposes a strict time-step limitation on the kinetics, which translates into a small spatial step (approximately $33\mu\text{m}$, equivalent to about 600 cells over the entire relaxation length for a constant-spacing grid). This becomes increasingly important as more of the upper levels are included as they tend to increase the slope of T_e just behind the shock.

D. Other Experiments

Results for cases 2–5 are provided in Fig. 8–11. Both the Mach 15.9 and 16.1 cases are in excellent agreement, which indicates that the numerical solution of the collisional-radiative is consistent. However, there is a slight under-prediction of the induction length for the Mach 16.5 case, and an over-prediction for the Mach 13 and 17.2 case. This non-monotonic behavior could not simply be explained from the collisional-radiative model. There are, however, several factors which can influence the experimental results. As noted by Enomoto³³, the boundary layer interaction with the shock structure initiates premature onset of the electron avalanche, thus shortening the overall relaxation length. Glass and Liu showed for a Mach 13.6 shock, the boundary layer significantly shortened the relaxation length more than 4 mm away from the wall. For the 5 cm diameter ANU shock tube, this represents a significant portion of the flow that would be affected by such a boundary layer. Another factor is the presence of impurities; as noted also by Glass and Liu¹¹ and verified by one-dimensional computations with a simplified model¹⁰, molecular impurities (including traces of water vapor) can have a strong effect in reducing the induction length. Both of these can be estimated with further computations, extending the scheme to include the Navier-Stokes equations for boundary layer development, and molecular chemistry. Yet another factor to consider is the unsteadiness of the flow; the experimental traces in figures 1 and 8–11 clearly show significant fluctuations. Accounting for the occasional shift in induction length, the computational profiles of the mass density and electron density or ionization fraction show a remarkable agreement with the mean of the experimental data. We will show in the companion paper that the flow exhibits very particular unsteady fluctuations, which lead to the observed profiles, as well as effects on the induction length which can bring our results closer to the experimental data.

Research on strongly ionizing shocks in argon were also carried out at the Australian National University (ANU) by Houwing *et al*³⁴, who was able to measure the population of the metastable states behind the shock through spatially-resolved hook interferometry. We also simulated these experiments, choosing similar flow conditions and using the same data-set of cross-sections.

The metastable populations behind a Mach 13.6 shock are presented in Figure 12(a), at the top. The current analysis accurately reproduces the peaks of both the $4s[3/2]_2$ and $4s'[1/2]_2$ curves as well as their slopes (the rate of decay) in the radiative cooling regime. Such agreement is only possible when the $4p$, $5s$, and $3d$ are included in the model in addition to the $4s$ levels, otherwise the population of the metastable states is greatly over-predicted as in Fig. 12(b), presenting yet another strong evidence for the ladder climbing process. The relaxation length in Figure 12(a), however, is again slightly over-predicted, even when experimental uncertainties are ac-

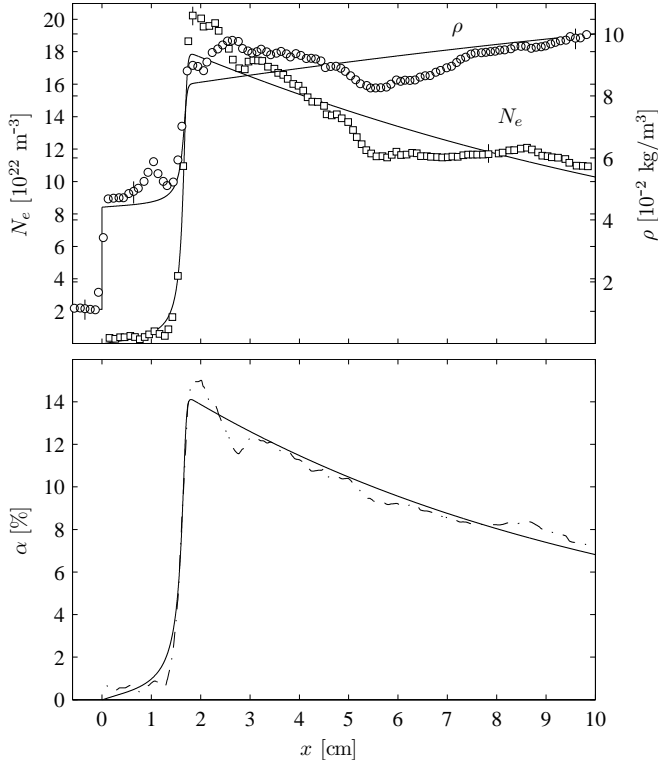


FIG. 8. Ionizing shock structure as detailed by (a) ρ and n_e , and (b) α for case 2: $p_o = 5.15$ torr, $T_o = 295.9$ K, $Ma = 16.1$.

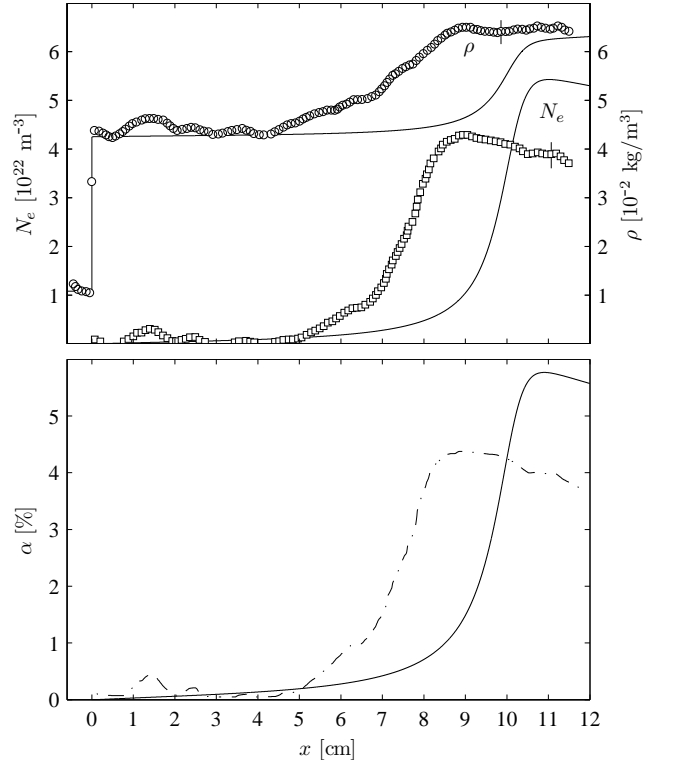


FIG. 10. Ionizing shock structure as detailed by (a) ρ and n_e , and (b) α for case 4: $p_o = 5.01$ torr, $T_o = 296.6$ K, $Ma = 13.0$.

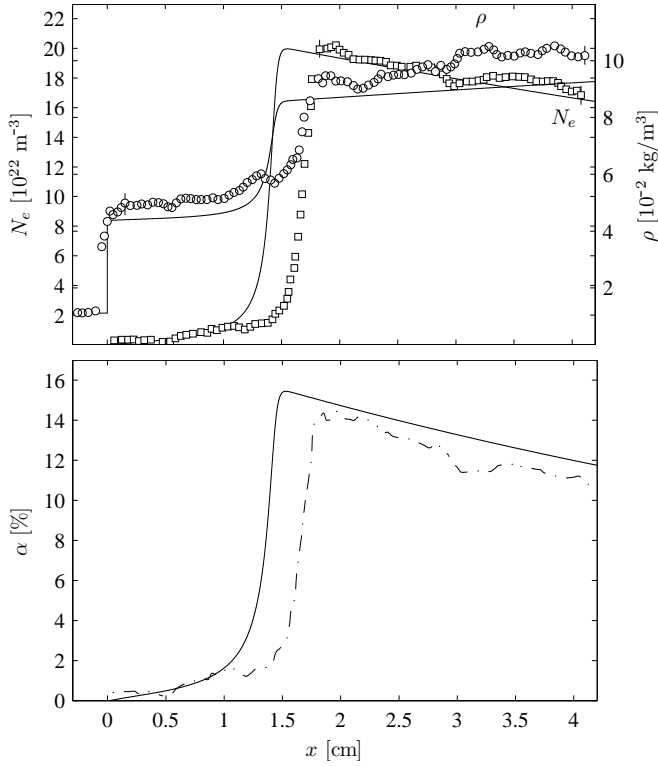


FIG. 9. Ionizing shock structure as detailed by (a) ρ and n_e , and (b) α for case 3: $p_o = 5.12$ torr, $T_o = 296.6$ K, $Ma = 16.5$.

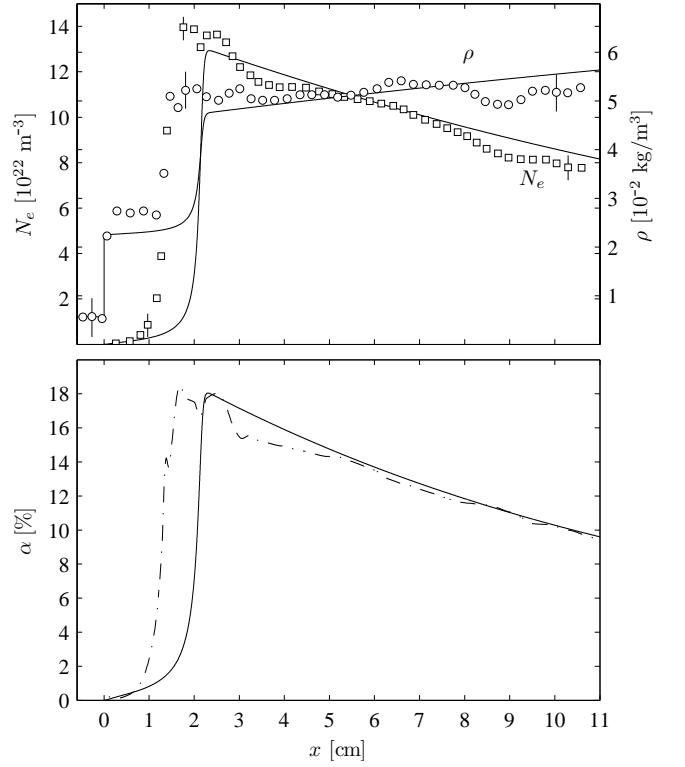


FIG. 11. Ionizing shock structure as detailed by (a) ρ and n_e , and (b) α for case 5: $p_o = 2.06$ torr, $T_o = 297.8$ K, $Ma = 17.2$.

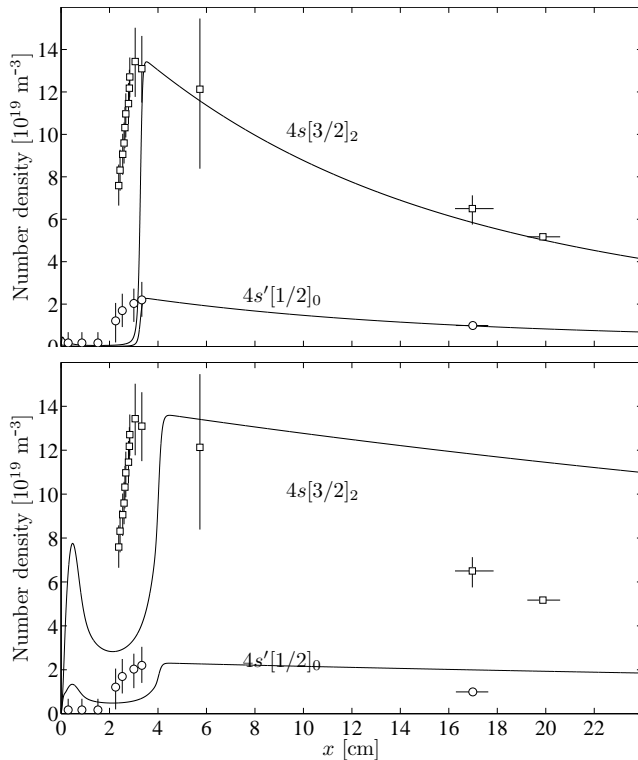


FIG. 12. Metastable populations behind a strongly ionizing shock traveling at 4.35 ± 0.5 km/s in pure argon at 10.0 ± 0.5 torr, 294 K.

counted for. In fact, the current analysis over-predicts the relaxation length for all cases presented by Houwing et al. when using the atom-atom impact cross sections calibrated for the UTIAS experiments. The reason for such a consistent error is likely due to the size of the shock tube used in the experiments, as noted earlier, i.e. the effect of developing boundary layers.

V. CONCLUSIONS

A detailed collisional-radiative model has been introduced which is able to accurately reproduce the structure of strongly ionizing shocks in argon. Comparison between steady-state computations and experimental shock-tube data in the Mach 13-18 range shows that the model provides a very good agreement with the density profiles and ionization fraction, and is able to reproduce the population of the metastable states, provided that the collisional-radiative model includes at least the 5s and 3d manifolds of neutral argon. We have also analyzed the respective contributions of the various elastic, inelastic and radiative exchange processes and shown strong evidence in support of the ladder climbing mechanism of ionization, in contrast to the two-step model of excitation to and ionization from the 4s manifold. Our simulations indicate that ionization proceeds more prevalently from the upper levels, and the ladder climbing process is also

more efficient as it results in reduced relaxation lengths. However, the inelastic collisions between the upper states is sufficiently rapid that a single excitation temperature could be considered a reasonable approximation in the induction region. Electron heat conduction has a negligible effect on the relaxation length, but can reduce time step limitations imposed by the kinetics in the electron priming region. While we have been able to validate the model against shock-tube data, there are remaining uncertainties; these will be addressed with further extension of the model. In a companion paper, we address two-dimensional and unsteady effects, while future work will include boundary layer effects and more detailed and complete kinetics, as well as radiation transport.

ACKNOWLEDGMENTS

We wish to acknowledge the support of the Air Force Office of Scientific Research (AFOSR), grant No. 02PR05COR (PM: Dr. F. Fahroo) for this work.

VI. REFERENCES

- ¹H. Petschek and S. Byron, "Approach to equilibrium ionization behind strong shock waves in argon," *Ann. Phys. (N.Y.)*, **1**, 270 (1957).
- ²L. Biberman and I. Yakubov, "Approach to ionization equilibrium behind the front of a shock wave in an atomic gas," *Soviet-Phys.-Tech. Phys. (English Transl.)*, **8**, 1001 (1964).
- ³H. D. Weymann, "...," *Tech. Rep. BN-144* (University of Maryland, Institute for Fluid Mechanics, 1958).
- ⁴P. H. Wojciechowski and H. D. Weymann, "Multistep initial ionization behind strong shock waves in argon," *Journal of Chemical Physics*, **61**, 1369 (1974).
- ⁵P. C. T. de Boer and P. R. Grimwood, "To be determined," *Bull. Am. Phys. Soc.*, **13**, 808 (1968).
- ⁶T. McLaren and R. Hobson, "Initial ionization rates in shock-heated argon, krypton, and xenon," *Phys. Fluids*, **11**, 2152 (1968).
- ⁷H. Mirels, *Physics of Fluids*, **6**, 1201 (1963).
- ⁸H. Mirels, *Physics of Fluids*, **9**, 1907 (1966).
- ⁹R. G. Shreffler and R. H. Christian, "Boundary disturbances in high-explosive shock tubes," *J. Appl. Phys.*, **25**, 324 (1953).
- ¹⁰J.-L. Cambier, "Numerical simulations of a nonequilibrium argon plasma in a shock-tube experiment," in *Proceedings of the 22nd Fluid Dynamics, Plasma Dynamics, and Lasers Conference* (AIAA, Honolulu, HI, 1991) pp. 1-20.
- ¹¹I. I. Glass and W. S. Liu, "Effects of hydrogen impurities on shock structure and stability in ionizing monatomic gases. Part 1. Argon," *J. Fluid Mech.*, **84**, 55 (1978).
- ¹²K. Harwell and R. Jahn, "Initial ionization rates in shock-heated argon, krypton, and xenon," *Phys. Fluids*, **7**, 1554 (1964).
- ¹³E. Morgan and R. Morrison, "Ionization rates behind shock waves in argon," *Phys. Fluids*, **8**, 1608 (1965).
- ¹⁴A. Kelly, "Atom-atom ionization cross sections of the noble gases—argon, krypton, and xenon," *J. Chem. Phys.*, **45**, 1723 (1966).
- ¹⁵H. Wong and D. Bershader, "Thermal equilibration behind an ionizing shock," *Journal of Fluid Mechanics*, **26**, 459 (1966).
- ¹⁶M. Merilo and E. Morgan, "Ionization rates behind shock waves in argon," *J. Chem. Phys.*, **52**, 2192 (1970).

- ¹⁷A. Kaniel, O. Igra, G. Ben-Dor, and M. Mond, "Ionization behind strong normal shock waves in argon," *Physics of Fluids*, **29**, 3618 (1986).
- ¹⁸S. Brassier and G. Gallice, "A Roe scheme for the bi-temperature model of magnetohydrodynamics," *Computers and Mathematics with Applications*, **41**, 257 (1998).
- ¹⁹J. Vlček, "A collisional-radiative model applicable to argon discharges over a wide range of conditions. I: Formulation and basic data," *J. Phys. D: Appl. Phys.*, **22**, 623 (1989).
- ²⁰A. Bultel, B. van Ootegem, A. Bourdon, and P. Vervisch, "Influence of Ar_2^+ in an argon collisional-radiative model," *Phys. Rev. E*, **65**, 1 (2002).
- ²¹K. Katsonis and H. W. Drawin, "Transition probabilities for argon(I)," *J. Quant. Spectrosc. Radiat. Transfer*, **23**, 1 (1980).
- ²²P. O. Haugsjaa and R. C. Amme, "Ionization and metastable excitation in low-energy collisions of ground state argon atoms," *J. Chem. Phys.*, **52**, 4874 (1970).
- ²³O. Zatsarinny and K. Bartschat, "*B*-spline Breit-Pauli *R*-matrix calculations for electron collisions with argon atoms," *J. Phys. B: At. Mol. Opt. Phys.*, **37**, 4693 (2004).
- ²⁴O. Zatsarinny and K. Bartschat, "*B*-spline calculations of oscillator strengths in neutral argon," *J. Phys. B: At. Mol. Opt. Phys.*, **39**, 2145 (2006).
- ²⁵H. Deutsch, K. Becker, A. N. Grum-Grzhimailo, K. Bartschat, H. Summers, M. Probst, S. Matt-Leubner, and T. D. Mark, "Calculated cross sections for the electron-impact ionization of excited argon atoms using the DM formalism," *Int. J. Mass Spectrom. Ion Process.*, **233**, 39 (2004).
- ²⁶H. Deutsch, K. Becker, S. Matt, and T. D. Mark, "Theoretical determination of absolute electron-impact ionization cross sections of molecules," *Int. J. Mass Spectrom. Ion Process.*, **197**, 37 (2000).
- ²⁷H. R. Griem, *Plasma Spectroscopy*, 1st ed. (McGraw-Hill, Inc., New York, 1964).
- ²⁸Y. B. Zel'dovich and Y. P. Raizer, *Physics of Shock Waves and High Temperature Hydrodynamic Phenomena*, 3rd ed. (Dover Publications, Inc., New York, 2002) ISBN 0-486-42002-7.
- ²⁹Y. Ralchenko, A. E. Kramida, J. Reader, and N. A. Team, "NIST atomic spectra database (version 3.1.5)," Tech. Rep. (NIST, 2008).
- ³⁰R. McEachran and A. Stauffer, "Relativistic effects in low-energy electron-argon scattering," *Aust. J. Phys.*, **50**, 511 (1997).
- ³¹M. Mitchner and C. H. Kruger, *Partially Ionized Gases*, 1st ed. (John Wiley and Sons, Inc., New York, 1973) ISBN 0-471-61172-7.
- ³²J. A. Bittencourt, *Fundamentals of Plasma Physics*, 3rd ed. (Springer-Verlag New York, Inc., New York, 2004).
- ³³Y. Enomoto, "Wall boundary effects on ionizing structure in argon," *Journal of the Physical Society of Japan*, **35**, 1228 (1973).
- ³⁴A. F. P. Houwing, T. J. McIntyre, P. A. Taloni, and R. J. Sandeman, "On the population of the metastable states behind unstable shock waves in ionizing argon," *J. Fluid. Mech.*, **170**, 319 (1986).